

Submitted to AJ (March 8, 2000)

Metallicity of Red Giants in the Galactic Bulge from Near-Infrared Spectroscopy

Solange V. Ramírez^{1,2}, Andrew Stephens, Jay A. Frogel¹, D. L. DePoy¹

Department of Astronomy, The Ohio State University

ABSTRACT

We present K -band spectra of more than 110 M giants in Galactic bulge fields interior to -4 degrees and as close as 0.2 degrees of the Galactic Center. From the equivalent widths of three features in these spectra, EW(Na), EW(Ca), and EW(CO) we calculate $[\text{Fe}/\text{H}]$ for the stars with a calibration derived from globular clusters (Stephens et al. 2000). The mean $[\text{Fe}/\text{H}]$ for each field is in good agreement with the results from Frogel et al. (1999) based on the slope of the giant branch method. We find no evidence for a metallicity gradient along the minor or major axes of the inner bulge ($R < 0.6$ kpc). A metallicity gradient along the minor axis, found earlier, arises when fields located at larger galactic radius are included. However, these more distant fields are located outside of the infrared bulge defined by the COBE/DIRBE observations.

We compute the $[\text{Fe}/\text{H}]$ distribution for the inner bulge and find a mean value of -0.21 dex with a full width dispersion of 0.30 dex, close to the values found for Baade's Window (BW) by Sadler et al. (1996) and to a theoretical prediction for a bulge formed by dissipative collapse (Mollá et al. 2000).

Subject headings: IR spectroscopy, stars: late-type, stars:giants

1. Introduction

Baade's Window (BW, $l = 1^\circ$, $b = -4^\circ$) is the most studied region in the Galactic bulge. In the late 1970s, Whitford (1978) demonstrated that the integrated optical spectrum from BW closely resembles that from bulges of spiral galaxies and from moderate luminosity E and S0 galaxies. At the same time Frogel et al. (1978) found that the near infrared light from these galaxies is dominated by cool giant stars. Shortly thereafter, Blanco and his collaborators determined that

¹Visiting Astronomer, Cerro Tololo Inter-American Observatory. CTIO is operated by AURA, Inc. under contract to the National Science Foundation.

²US Gemini Fellow

BW contains an unusually high percentage of middle and late type M giants compared to other regions of the Galaxy (Blanco et al. 1984). Detailed studies of the M giants in BW revealed that they have photometric and spectroscopic properties significantly different from those of M giants in the field (Frogel & Whitford 1987; Frogel 1988; Frogel et al. 1990; Rich 1983, 1988; Terndrup et al. 1990; McWilliam & Rich 1994).

The accurate determination of stellar metallicities is essential for constraining models of star formation and chemical evolution in the bulge. Frogel et al. (1990) used *JHK* colors and CO and H₂O photometric indices to determine metallicities of stars at latitudes between -3° and -12° along the minor axis. Tiede et al. (1995) used the relation between the slope of the upper giant branch and [Fe/H] (Kuchinski et al. 1995; Kuchinski & Frogel 1995) to estimate metallicities for the same stars studied by Frogel et al. (1990). Tyson (1991) used Washington photometry on stars in similar fields for the same purpose. These three studies agreed that there is a small metallicity gradient along the minor axis of the bulge, with values ranging from -0.04 dex/deg (Frogel et al. 1990) to -0.09 dex/deg (Tyson 1991). Finally, Minniti et al. (1995) discussed evidence for a metallicity gradient in the Galactic bulge based on compiled observations of ten fields, eight of them exterior to BW.

Stars in most of the inner bulge ($|b| \leq 3^\circ$) can be studied only with near infrared observations because of high reddening and extinction. Recently, Frogel et al. (1999) have studied 11 fields in the inner Galactic bulge using *JHK* photometry. Seven of these fields are on the minor axis; five are at a latitude of -1.3° parallel to the major axis. They estimated the reddening of each field from their CMDs and the mean metallicity of each field with the giant branch slope method. They combined their results with those of Tiede et al. (1995) and derived a gradient of -0.064 ± 0.012 dex/degree in the range $-0.2^\circ \leq b \leq -10.25^\circ$ along the minor axis.

Our main goal is to obtain independent values for the metallicity of the stars in the same inner bulge fields studied by Frogel et al. (1999) but with spectroscopic techniques. We use the strength of three absorption features present in the *K*–band of cool stars: Na, Ca, and CO. The calibration is based on similar observations of giants in globular clusters by Stephens et al. (2000).

2. Observations and Data Reduction

2.1. Observations

The observations for this paper were obtained on the 4m Blanco telescope at Cerro Tololo Inter-American Observatory (CTIO) during three observing runs with two instruments: the Ohio State InfraRed Imager and Spectrograph (OSIRIS; $R = 1380$; DePoy et al. 1993), and the CTIO InfraRed Spectrograph (IRS; $R = 1650, 4830$; DePoy et al. 1990). OSIRIS used a 256×256 NICMOS3 detector and IRS has a 256×256 InSb array. Spectral coverage was between $2.19 \mu\text{m}$ and $2.32 \mu\text{m}$ with both instruments. Table 1 gives a brief log of the observing runs.

Program stars were selected from the color magnitude diagrams of 11 fields interior to -4 degrees and as close as 0.2 degrees to the Galactic Center (Frogel et al. 1999). All of the observed stars are at or near the top of the red giant branch of each field. Based on their location in the CMDs we believe their probability of membership in the bulge is high. Fields are designated as in Frogel et al. (1999). Our sample also includes 14 stars in BW from Frogel & Whitford (1987) and Terndrup et al. (1991). Table 2 lists our final sample of stars. Column 1 gives the star’s name, column 2 the date of observation (year, month, day), column 3 the spectral resolution, column 4 the estimated S/N ratio per pixel in the spectrum, columns 5 and 6 the observed K magnitude and $J - K$ colors (Frogel et al. 1999, and unpublished), columns 7 and 8 the absolute K magnitude and dereddened $J - K$ colors (see section 3.2), and columns 9, 10 and 11 the equivalent widths of the Na, Ca, and CO features. The tabulated uncertainties in these three quantities are simply the ratio of the mean continuum to the rms noise present in the defined continuum regions (see section 3.1).

2.2. Data Reduction

The data acquisition and reduction were similar for all the spectra. Both instruments, OSIRIS and IRS, were used first in imaging mode to acquire the star in the slit. We took several spectra (~ 10) with the star stepped along the slit. This was done to estimate the sky levels in the exposures, to compensate for bad pixels, and to aid in the removal of the fringes present in the OSIRIS data which are typically ~ 6 % (peak-to-peak) of the continuum. A star of spectral type A or B was observed as close to the object star’s airmass as possible to correct for telluric absorption features. Such stars have no significant spectral features in the wavelength region we observed. After we averaged the multiple spectra of a program star and divided by the average spectrum of the nearby atmospheric standard star, the fringes cancelled to $< 1\%$. OSIRIS and IRS at $\lambda/\Delta\lambda = 1650$ can cover the entire relevant spectral region ($2.19\mu\text{m} - 2.34\mu\text{m}$) with a single grating setting; with IRS at $\lambda/\Delta\lambda = 4830$, however, we observed at three overlapping grating settings ($2.191\mu\text{m} - 2.242\mu\text{m}$, $2.238\mu\text{m} - 2.290\mu\text{m}$, and $2.285\mu\text{m} - 2.337\mu\text{m}$) to cover the desired wavelength range. A number of stars were observed at both grating settings as a quality control check. We will discuss results of this check later.

We used Image Reduction and Analysis Facility (IRAF) software for data reduction. The reduction process consisted of flat fielding the individual spectra with dome flats and sky subtraction using a sky frame made by a median combination of all data frames of the object. We replaced bad pixels (dead pixels and cosmic ray hits) by an interpolated value computed from neighboring pixels in the dispersion direction. The OSIRIS frames were then geometrically transformed to correct the curvature of the slit induced by the grating (maximum correction ~ 2 pixels). The induced curvature in IRS frames was insignificant (< 1 pixel) over the region of the array that was used. Geometric transformations for OSIRIS were derived from night sky emission lines. We extracted the individual spectra along an aperture of 7 pixels using the APSUM package in IRAF and did a further sky

subtraction by using regions on either side of the aperture. The final spectrum is an average of the extracted spectra. We divided the spectra of object stars by an early type atmospheric standard star, observed and reduced in the same way, to remove telluric absorption features and multiplied by a 10,000 K blackbody to put the spectra on a F_λ scale. The temperature of the blackbody approximately corresponds to the average temperature of our atmospheric standard stars. The maximum effect from the difference between the standard star temperature and the temperature of the adopted 10,000 K blackbody is a $\sim 1.5\%$ tilt in the continuum slope, which is insignificant to the equivalent width measurements.

We used OH air-glow lines (Olivia & Origlia 1992) to obtain wavelength solutions. For OSIRIS and IRS at $R = 1650$ spectra, we also included the $^{12}\text{CO}(2,0)$ bandheads near zero radial velocity to compute the wavelength calibration since there are no OH air-glow lines present at the red end of the K -band spectra. OH air-glow lines were present only in the first grating setting ($2.191\mu\text{m} - 2.242\mu\text{m}$); a second-order wavelength solution was derived there. Since the grating is the same for the three grating settings and the grating angle differences are small, the first and second order terms of the first grating setting solution should be the same for all three observed grating settings. After applying those terms to the second ($2.238\mu\text{m} - 2.290\mu\text{m}$) and third ($2.285\mu\text{m} - 2.337\mu\text{m}$) grating settings, only the zero order term is unknown. This zero order term is just a shift that was computed from the lines present in the overlapping regions. We connected the three grating settings, after wavelength calibration, by averaging the overlapping regions.

We shifted both the OSIRIS and IRS spectra in wavelength to correct for radial velocity differences; the $^{12}\text{CO}(2,0)$ bandhead was fixed at $2.293\mu\text{m}$. This shift is needed to ensure the relative accuracy and consistency of the equivalent widths of atomic and molecular features. A sample of the final normalized spectra are shown in Figures 1 on an F_λ scale. Only the brightest stars for each field are shown in the Figures. The whole database is available on the anonymous FTP site of the OSU Astronomy Department (`ftp to ftp.astronomy.ohio-state.edu`, login as `anonymous`, change to `directory pub/solange`, and get the file `bulge_spec.tar.gz`).

3. Analysis

3.1. Equivalent Widths of Atomic and Molecular Absorption Features

Stellar photospheric absorption features in our spectra were identified from the wavelengths of the lines in Kleinmann & Hall (1986). The strongest features in our data are lines of Na I and Ca I, and the (2,0) bands of ^{12}CO . The equivalent widths of these features were measured with respect to a continuum level defined as the best first-order fit for bands free of spectral lines near the features. The band passes adopted for the features and continuum are given in Table 3 and the features themselves are shown in Figure 1. These bandpasses are identical to those used to measure the giants stars in globular clusters (Stephens et al. 2000). The measured equivalent widths for Na I, Ca I, and $^{12}\text{CO}(2,0)$ for our program stars are listed in Table 2.

To estimate the *formal* uncertainties, we assume that the noise is dominated by photon statistics and that $\sigma_{\text{line}} \sim \sigma_{\text{cont}}$. The uncertainty in the measurement of each feature (in Å) is given by:

$$\sqrt{2N_{\text{pixels}}} \times \text{dispersion} \times \sigma_{\text{cont}}$$

where N_{pixels} is the number of pixels contained within the defined feature band, dispersion is measured in Å per pixel, and σ_{cont} is the rms noise per pixel of the fitted continuum. Uncertainties listed in Table 2 were calculated using this formula. These values are really lower limits as they provide no estimate for any systematic errors that may exist in the data. More realistic estimates of the uncertainties are computed below, using differences found in measurements taken with different instruments and spectral resolutions.

Each feature at each resolution has its own calculated rms noise. The estimated signal-to-noise ratio that appears in Table 2 is the ratio of the continuum level to the standard deviation of each spectrum. The standard deviation of each spectrum is the quadratic average of the calculated rms noise of each feature ($\sigma_{\text{cont}} = \sqrt{[\sigma_{\text{cont}}^2(\text{Na}) + \sigma_{\text{cont}}^2(\text{Ca}) + \sigma_{\text{cont}}^2(\text{CO})]/3}$).

There are 13 stars with IRS spectra at both spectral resolutions 1650 & 4830. Also, there are 8 stars with spectra taken with OSIRIS at R=1380 and IRS at R=1650. The average differences and standard deviation of Na, Ca, and CO equivalent widths measured at both resolutions are listed in Table 4. The last column of Table 4 is the average formal error from Table 2. The mean differences of the equivalent widths measured at different resolutions and taken with different instruments are negligible at the one sigma level. Thus, when we have more than one observation we will use the average of the equivalent widths measured at different resolutions. The standard deviations listed in Table 4 are also an indicator of potential systematic uncertainties in the data; we consider these values to be a better estimate of the true uncertainties in the respective equivalent widths than the formal errors. The total uncertainties are computed as the average of the standard deviations listed in Table 4, and are 0.38 for EW(Na), 0.87 for EW(Ca) and 1.7 for EW(CO).

3.2. Reddening

We estimated the extinction and reddening to each star using the same technique as Frogel et al. (1999). Specifically, we assumed that the color of the upper giant branch in each field was the same as that in BW:

$$(J - K)_0 = -0.113K_0 + 2.001 \tag{1}$$

where $(J - K)_0$ is the dereddened $J - K$ color and K_0 is the dereddened K magnitude. Further, we assumed the relation between extinction and reddening found by Mathis (1990):

$$A_K = 0.618E(J - K). \tag{2}$$

The reddening is estimated by calculating the shift in K and $J - K$ along the reddening vector to force each star to fall on the BW giant branch. M_{K_0} is computed assuming that all stars are

located at a distance of 8 kpc. Dereddened photometric indices, M_{K_0} and $(J - K)_0$, are listed in Table 2.

The photometric uncertainties are estimated to be about 0.04 or 0.05 magnitudes (Frogel et al. 1999) for K and $(J - K)$. The uncertainties of the dereddened photometric indices should also include the uncertainties caused by the differential reddening present in each field and the assumption that all stars are located at the same distance. Frogel et al. (1999) found that the amount of scatter due to differential reddening is proportional to the average reddening for each field. Using eq. (3) from Frogel et al. (1999) we estimate that the scatter due to differential reddening implies a scatter in $(J - K)_0$ of 0.30 mag for the c fields and 0.12 mag for the g fields, and a scatter in M_{K_0} of 0.2 mag for the c fields and 0.1 mag for the g fields and BW. The maximum dispersion in magnitude due to spread along the line of sight is 0.2 mag (Frogel et al. 1990) for fields at galactic latitude less than 4° . So, the scatter in M_{K_0} including both the effects of differential reddening and dispersion along the line of sight is 0.30 mag for the c fields and 0.23 mag for the g fields and BW.

4. Results

4.1. Dependence on Luminosity

Figure 2 shows the dependence of the equivalent widths of Na, Ca, and CO on M_{K_0} . These plots resemble CMDs, since the EW(Na), EW(Ca), and EW(CO) may depend on both effective temperature and luminosity in addition to metallicity.

There is a considerable amount of scatter in Figure 2. We computed the standard deviation of EW(Na), EW(Ca), and EW(CO) in two narrow ranges of M_{K_0} , listed in Table 5, to minimize any spread that might arise from an M_{K_0} dependence of the indices. In all cases the standard deviation is greater than the total uncertainties of the equivalent widths (see Sec. 3.1). Therefore, part of the scatter is real and can be understood as a spread in metallicity in our sample of bulge stars. Note that we assume all stars are of closely similar age so that only [Fe/H] differences will cause a spread in color or EW at a given M_{K_0} . If the observed scatter is the quadratic addition of the scatter due to differences in metallicity and the scatter due to uncertainties in the data, then the scatter due to metallicity is 0.9 Å for EW(Na), 0.4 Å for EW(Ca), and 1.8 Å for EW(CO).

There is a statistically significant slope of -0.6 Å/mag in EW(CO) vs. M_{K_0} . However, this probably reflects the dependence of both EW(CO) and M_{K_0} on $(J - K)_0$ color (see Johnson 1966; Ramírez et al. 1997). In particular, as giants evolve they increase in luminosity and decrease in effective temperature. As the effective temperature decreases, the CO opacity, and hence the strength of the CO lines, increases. For example, there is a slope of ~ -0.5 Å/mag in the EW(CO) vs. M_{K_0} relation for the field giants, assuming that the giant branch of BW (eq. 1) is similar to the giant branch of field giants. This is very similar to the slope of -0.6 Å/mag we observe.

This suggests that the slope we observe in $\text{EW}(\text{CO})$ vs. M_{K_0} in Figure 2 can be explained by the dependence of both $\text{EW}(\text{CO})$ and M_{K_0} on effective temperature or $(J - K)_0$ color.

There is no obvious relation between $\text{EW}(\text{Na})$ and $\text{EW}(\text{Ca})$ with respect to M_{K_0} . Our previous study of field giants (Ramírez et al. 1997) indicates that such a relation should exist (for the same reasons as for CO). But, the scatter is too high in the graphs of $\text{EW}(\text{Na})$ and $\text{EW}(\text{Ca})$ vs. M_{K_0} to find a relationship between those indices.

4.2. Metallicity using Globular Cluster Giants

Stephens et al. (2000) have established an $[\text{Fe}/\text{H}]$ scale for Galactic globular clusters based on medium resolution (1500-3000) infrared K band spectra of the brightest stars in 15 clusters. The technique uses the same absorption features as we use here: Na, Ca, and CO. Indeed, many of their spectra were obtained with the identical instrument set up and on the same nights as the spectra analyzed here. Their calibration is derived from spectra of more than 100 giant stars in 15 Galactic globular clusters which have good optical abundance determinations. The technique is valid for globular cluster giants with $-1.8 < [\text{Fe}/\text{H}] < -0.1$ and $-7 < M_{K_0} < -4$, and has a typical uncertainty of ± 0.1 dex.

Our sample of stars in the different bulge fields has similar colors and magnitudes to the stars analyzed by Stephens et al. (2000). Figure 3 shows the color-magnitude diagram for the globular cluster stars from Stephens et al. (2000) and our sample of bulge stars with $M_{K_0} > -7$. The scatter seen in globular cluster stars is real and arises from sequences of different metallicities, where bluer cluster stars are more metal poor. The bulge stars appear in a line because of the dereddening technique, where we force the stars to lie on the BW giant branch. Figure 4 compares the three spectral indices ($\text{EW}(\text{Na})$, $\text{EW}(\text{Ca})$, and $\text{EW}(\text{CO})$) with dereddened color, $(J - K)_0$ for globular cluster and bulge stars. Note that there is considerable overlap of the two populations although the globular cluster stars extend to lower values of equivalent widths while the bulge stars go to higher values. These differences most likely reflect differences in the $[\text{Fe}/\text{H}]$ distributions of the two populations.

Stephens et al. (2000) calculated two calibrations for globular cluster metallicities. Solution 1 estimates the metallicity with only the spectral indices $\text{EW}(\text{Na})$, $\text{EW}(\text{Ca})$, and $\text{EW}(\text{CO})$. Solution 2 also incorporates the dereddened $(J - K)$ color and the absolute K -band magnitude. Figure 5 shows a comparison between results of solution 1 and 2 for the globular cluster and bulge stars. The two solutions yield indistinguishable results for the globular cluster stars, but for stars in the bulge, solution 2 gives higher metallicities for $[\text{Fe}/\text{H}] > -0.2$. Both solutions are extrapolations for $[\text{Fe}/\text{H}]$ values higher than -0.15 . Nevertheless, we would like to understand which solution might be better to use as an extrapolation to the higher metallicities. At higher metallicities the $\text{EW}(\text{CO})$ reaches a plateau and become insensitive to changes in $[\text{Fe}/\text{H}]$ (Stephens et al. 2000). Since solution 1 has a stronger dependence on the $\text{EW}(\text{CO})$ than solution 2, solution 1 is expected to be less sensitive

to changes in $[\text{Fe}/\text{H}]$ at higher metallicities. The analysis of Stephens et al. (2000) also shows that at higher metallicities M_{K_0} accounts for more and more of the variation in $[\text{Fe}/\text{H}]$. For this reason we feel that solution 2 is a better indicator of metallicity, and is the one we applied to our sample of bulge stars.

We applied solution 2 to the individual stars of our sample with $M_{K_0} \geq -7$, corresponding to the brightest cluster stars. If we consider a typical bulge star of $M_{K_0} = -6.5$, $(J - K)_0 = 1.1$, $\text{EW}(\text{Na}) = 4.0 \text{ \AA}$, $\text{EW}(\text{Ca}) = 3.0 \text{ \AA}$, $\text{EW}(\text{CO}) = 21.9 \text{ \AA}$, the total uncertainties for the equivalent widths (see section 3.1), and the scatter in the photometric indices due to differential reddening and dispersion through the line of sight (see section 3.2), we compute a typical error in $[\text{Fe}/\text{H}]$ of ± 0.12 dex for individual stars in the g fields and BW and ± 0.23 dex for individual stars in the c fields. The typical error in $[\text{Fe}/\text{H}]$ is almost doubled for the stars in the c fields, because differential reddening is higher in these very low latitude fields and the uncertainty in the $(J - K)_0$ color becomes important.

We compute a mean value of $[\text{Fe}/\text{H}]$ for each field by averaging the results of the individual stars. The mean $[\text{Fe}/\text{H}]$, the standard deviation and the error in the mean for each field are listed in Table 6. The error in the mean is the standard deviation divided by the square root of the number of stars in each field.

5. Discussion

5.1. Comparison to Slope of Giant Branch method.

Frogel et al. (1999) used the slope of the giant branch (GB) to estimate the mean metallicities of the same c and g fields of our sample. For BW we used the slope of the GB result from Tiede et al. (1995). In Figure 6 we have plotted slope of the GB results against ours. The agreement is very good in all the fields, except for g3-1.3. The mean average difference of both techniques is -0.03 ± 0.15 dex, entirely consistent with the combined uncertainties of the two techniques.

5.2. Metallicity Gradients in the Inner Bulge.

We first explore the possible existence of a metallicity gradient along the major-axis of the inner bulge including all the fields with galactic latitude, $b = -1.3^\circ$. Figure 7 shows our results for g0-1.3, g1-1.3, g1-1.3, g2-1.3, and g4-1.3 fields plotted against galactic longitude, l . The line is an error weighted least-squares fit to the points. We find that there might be a small metallicity gradient along the major axis since the slope of the line is 0.017 ± 0.011 dex/degree. In Figure 7, we have also plotted the metallicity gradient along the major axis obtained by Frogel et al. (1999) (dashed-line). Note that their result and ours are very close.

Next we explore the existence of a metallicity gradient along the minor-axis of the inner bulge including all the fields with galactic longitude, $l \sim 0^\circ$. Figure 8 shows our results for c, g0-1.3, g0-1.8, g0-2.3, g0-2.8, and BW fields plotted against galactic latitude, b . The line is an error weighted least-squares fit to the points. There is no evidence for a metallicity gradient along the minor axis; the slope of the fit is -0.012 ± 0.027 dex/deg. This result seems to be in disagreement with earlier results, in which a metallicity gradient along the minor axis ranges from -0.04 dex/deg (Frogel et al. 1990) to -0.09 dex/deg (Tyson 1991). However, if we consider only the metallicities obtained by Frogel et al. (1999) for the c, g0-1.3, g0-1.8, g0-2.3, g0-2.8, and BW fields we obtain a fit with a slope of 0.001 ± 0.021 , in close agreement with our spectroscopic result. The minor axis metallicity gradient found in earlier studies arises when fields at higher galactic latitude are also included. In Figure 8, we have plotted as a dashed line the metallicity gradient along the minor axis obtained by Frogel et al. (1999) including all fields with $l \leq 10.5^\circ$.

In Figure 9, we have plotted the location of the observed fields with respect to a $3.5\mu\text{m}$ COBE/DIRBE outline of the Galactic bulge (Weiland et al. 1994). When only fields located inside the COBE/DIRBE outline are considered, no metallicity gradient is found. The metallicity gradient arises only when fields located outside the COBE/DIRBE outline ($R > 0.6$ kpc) are included. Metallicity gradients in the galactic bulge have recently been predicted by the theoretical models of Mollá et al. (2000). Mollá et al. present a multiphase evolution model which assumes a dissipative collapse of the gas from a protogalaxy or halo to form the bulge and the disk. They predict a metallicity gradient of -0.4 dex/kpc in the bulge region $0.5 \leq R \leq 1.5$ kpc, which is in good agreement with the metallicity gradient found by Frogel et al. (1999). But, Mollá et al. also predict a steeper gradient, -0.8 dex/kpc, in the inner bulge at $R < 0.5$ kpc, which is not observed in our data or in the Frogel et al. (1999) data. We find the metallicity gradient becomes flat at the scale height where the infrared light becomes dominant in the Galactic bulge ($R < 0.6$ kpc). Mollá et al. (2000) assume that a core population, which is metal rich and supported by rotation, dominates the stellar population of the inner bulge. The existence of such a metal rich population in the inner bulge is not supported by recent measurements of stellar iron abundances in the Galactic Center by Ramírez et al. (2000), who found $[\text{Fe}/\text{H}]$ near solar for a sample of late supergiant and giant stars.

5.3. $[\text{Fe}/\text{H}]$ metallicity distribution

In section 4.1 we found that the spread in EW(Na, Ca, CO) at a given magnitude was consistently higher than expected from measurement uncertainties alone. A likely explanation for the observed spread in the equivalent width values is that it arises from an intrinsic spread in $[\text{Fe}/\text{H}]$ for the stars.

We compute the $[\text{Fe}/\text{H}]$ metallicity distribution considering all stars in our sample with $M_{K_0} \geq -7$ but excluding the c field stars, because of their large individual uncertainties in $[\text{Fe}/\text{H}]$, and including stars along the major axis, for a total of 72 stars. The mean $[\text{Fe}/\text{H}]$ for the inner bulge

is -0.21 dex with a full width dispersion of 0.30 dex. Since the average error of our $[\text{Fe}/\text{H}]$ results is ± 0.12 per star (see section 4.2), the dispersion observed in the metallicity distribution is real. These values are consistent with theoretical results from Mollá et al. (2000), who predict a mean $[\text{Fe}/\text{H}]$ of -0.20 with a dispersion of 0.40 dex for one bulge population recipe. If we consider a typical bulge star of $M_{K_0} = -6.5$, $(J - K)_0 = 1.1$, $\text{EW}(\text{Na}) = 4.0 \text{ \AA}$, $\text{EW}(\text{Ca}) = 3.0 \text{ \AA}$, $\text{EW}(\text{CO}) = 21.9 \text{ \AA}$, compute $[\text{Fe}/\text{H}]$ using solution 2 of Stephens et al. (2000), and determine the difference in $[\text{Fe}/\text{H}]$ adding and subtracting the scatter in the equivalent widths due to metallicity (see Sec. 4.1), we obtain a difference of ± 0.26 . This number is very similar to the dispersion of the $[\text{Fe}/\text{H}]$ distribution. We conclude that the scatter seen in the equivalent widths is real and can be explained by the dispersion observed in the $[\text{Fe}/\text{H}]$ distribution.

We now compare the metallicity distribution of our sample of 72 stars in the inner bulge with the metallicity distribution derived for BW by Sadler et al. (1996) in Figure 10. Their mean $[\text{Fe}/\text{H}]$ for 262 stars in BW is -0.15 dex with a dispersion of 0.44 dex. This is quite similar to our mean of -0.21 dex with a dispersion of 0.30 dex.

6. Conclusions.

We present K -band spectra of giant stars in fields interior to -4 degrees and as close as 0.2 degrees of the Galactic Center. We measure equivalent widths of the strongest features present in the K -band spectra, $\text{EW}(\text{Na})$, $\text{EW}(\text{Ca})$, and $\text{EW}(\text{CO})$, and also dereddened photometric indices M_{K_0} and $(J - K)_0$. We use these indices to compute $[\text{Fe}/\text{H}]$ for the individual stars, using the calibration derived for globular clusters by Stephens et al. (2000). The mean $[\text{Fe}/\text{H}]$ for each field is in good agreement with the results obtained with the slope of the giant branch method (Frogel et al. 1999). We find no evidence for a metallicity gradient along the minor or major axis of the bulge for $R < 0.6$ kpc. We also show that metallicity gradients found in earlier works only arise when fields located at larger galactic radii are included. Those higher galactic radii fields are located outside the infrared bulge defined by the COBE/DIRBE outline. We compute the $[\text{Fe}/\text{H}]$ distribution for the inner bulge, finding a mean value of -0.21 dex with a full width dispersion of 0.30 dex, which are very similar to the mean and width of the BW's $[\text{Fe}/\text{H}]$ distribution from Sadler et al. (1996) and to the theoretical distribution of a bulge formed by dissipative collapse (Mollá et al. 2000).

S.V.R. gratefully acknowledges support from a Gemini Fellowship (grant # GF-1003-97 from the Association of Universities for Research in Astronomy, Inc., under NSF cooperative agreement AST-8947990 and from Fundación Andes under project C-12984), and from an Ohio State Presidential Fellowship. We thank the CTIO staff for helpful support. J.A.F. thanks the former director of the Carnegie Observatories, Dr. Leonard Searle, for a Visiting Research Associateship without which this program could not have gotten started. Finally, J.A.F. notes that NSF declined to provide support for this research program.

REFERENCES

- Blanco, V. M., McCarthy, M. F., Blanco, B. M. 1984, *AJ*, 89, 636
- DePoy, D. L., Gregory, B., Elias, J., Montane, A., & Perez, G., 1990, *PASP*, 102, 1433
- DePoy, D. L., Atwood, B., Byard, P., Frogel, J. A., & O'Brien, T. 1993, in *Infrared Detectors and Instrumentation*, SPIE vol. 1945 (Bellingham: SPIE), 667
- Frogel, J. A. 1988, *ARA&A*, 26, 51
- Frogel, J. A., Persson, S. E., Aaronson, M., Matthews, K. 1978, *ApJ*, 220, 75
- Frogel, J. A. & Whitford, A. E., 1987, *ApJ*, 320, 199
- Frogel, J. A., Terndrup, D. M., Blanco, V. M., & Whitford, A. E., 1990, *ApJ*, 353, 494
- Frogel, J. A., Tiede, G., Kuchinski, L. E., 1999, *AJ*, 117, 2296
- Johnson, H. L. 1966, *ARA&A*, 4, 193
- Kleinmann, S. G. & Hall, D. N. B. 1986, *ApJS*, 62, 501
- Kuchinski, L. E., Frogel, J. A., Terndrup, D. M., & Persson, S. E. 1995, *AJ*, 109, 1131
- Kuchinski, L. E. & Frogel, J. A., 1995, *AJ*, 110, 2844
- Mathis, J. S. 1990, *ARA&A*, 28, 37
- McWilliam, A. & Rich, R. M., 1994, *ApJS*, 911, 749
- Minniti, D., Olszewski, E. W., Liebert, J., White, S. D. M., Hill, J. M., & Irwin, M. J., 1995, *MNRAS*, 277, 1293
- Mollá, M., Ferrini, F., & Gozzi, G., 2000, *MNRAS*, in press
- Oliva, E. & Origlia, L. 1992, *A&A*, 254, 466
- Ramírez, S. V., DePoy, D. L., Frogel, J. A., Sellgren, K., & Blum, R. D., 1997, *AJ*, 113, 1411
- Ramírez, S. V., Sellgren, K., Carr, J. S., Balachandran, S. C., Blum, R., Terndrup, D. M., & Steed, A., 2000, *ApJ* in press
- Rich, R. M., 1983 Ph.D. thesis, UCSC
- Rich, R. M. 1988, *AJ*, 96, 884
- Sadler, E. M., Rich, R. M., & Terndrup, D. M., 1996, *AJ*, 112, 171
- Stephens, A., Frogel, J. A., & Ramírez, S. V., 2000, in preparation

Terndrup, D. M., Frogel, J. A., & Whitford, A. E., 1990, *ApJ*, 357, 453

Terndrup, D. M., Frogel, J. A., & Whitford, A. E., 1991, *ApJ*, 378, 742

Tiede, G. P., Frogel, J. A., & Terndrup, D. M., 1995, *AJ*, 110, 2788

Tyson, N. D. 1991, Ph.D. thesis, Columbia University

Weiland, J. L., Arendt, R. G., Berriman, G. B., Dwek, E., Freudenreich, H. T., Hauser, M. G., Kelsll, T., Lisse, C. M., Mitra, M., Moseley, S. H., Odegard, N. P., Silverberg, R. F., Sodroski, T. J., Spiesman, W. J., & Stemwedel, S. W., 1994, *ApJ*, 425, L81

Whitford, A. E., 1978, *ApJ*, 226, 777

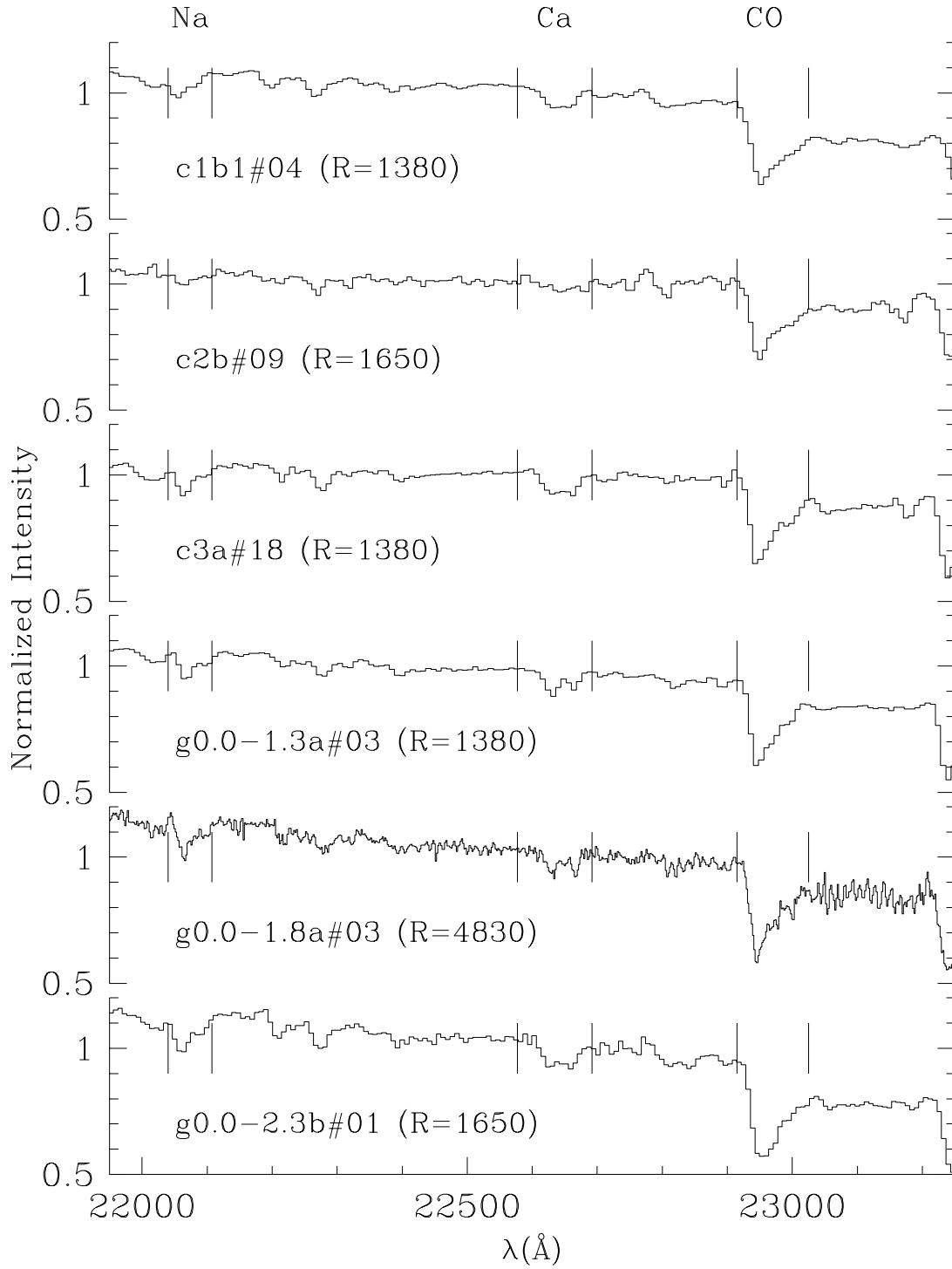
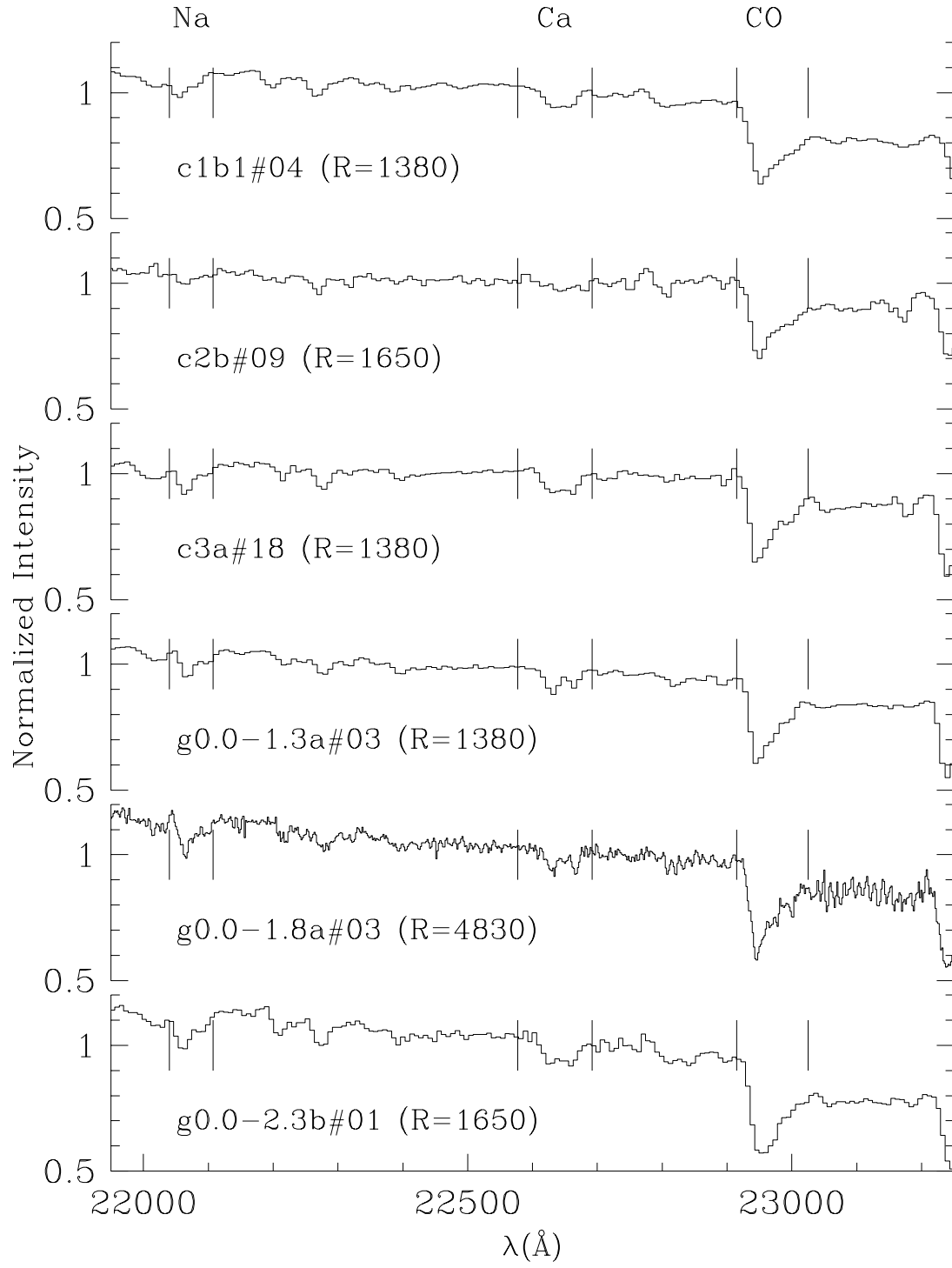


Fig. 1.— Spectra of the brightest stars at each field presented as normalized flux (F_λ). Each star is identified below its spectrum. The vertical bars show the limits of the feature bands.



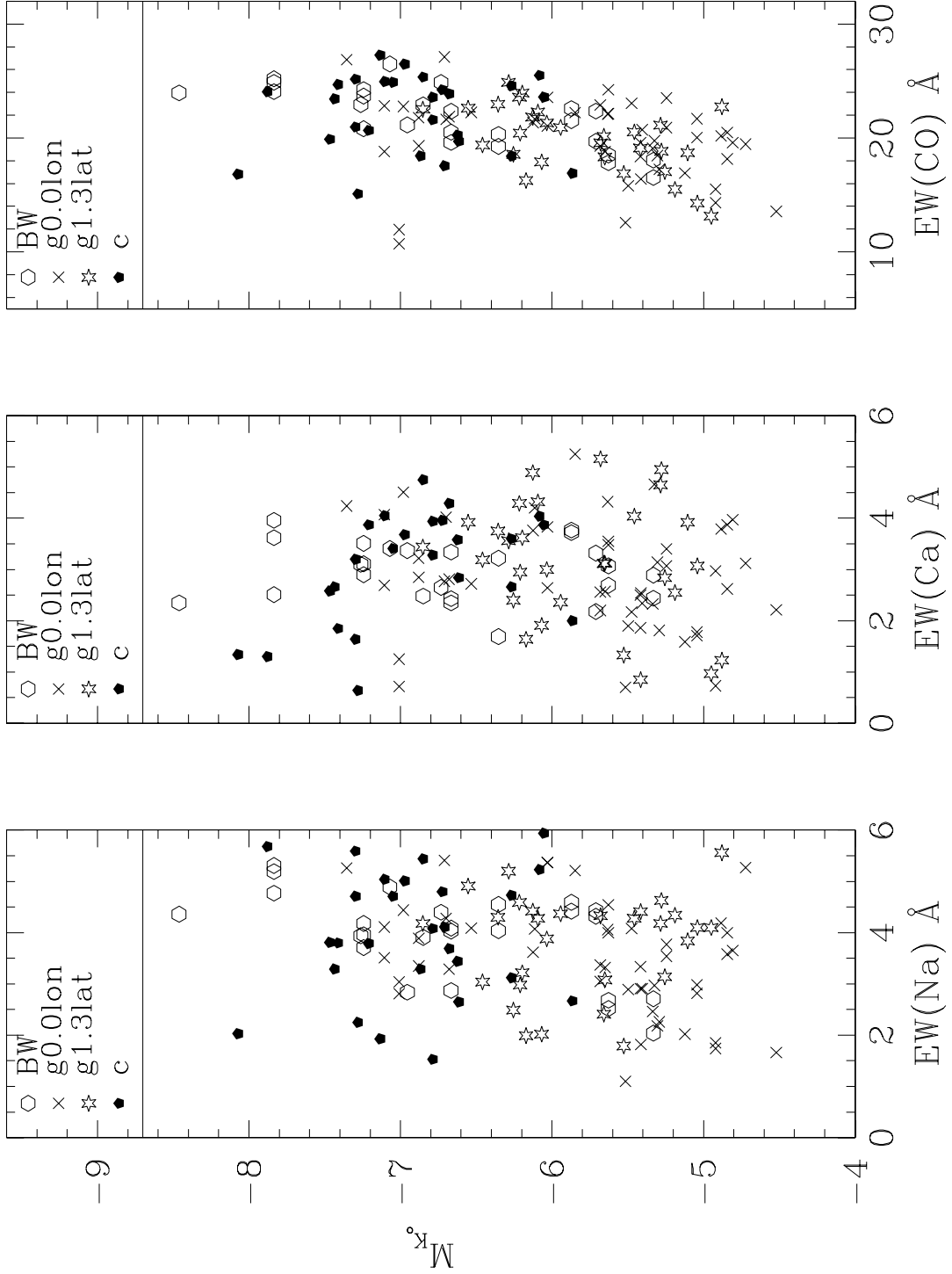


Fig. 2.— Equivalent widths of the spectral features Na, Ca, and CO plotted against absolute magnitude, M_{K_0} .

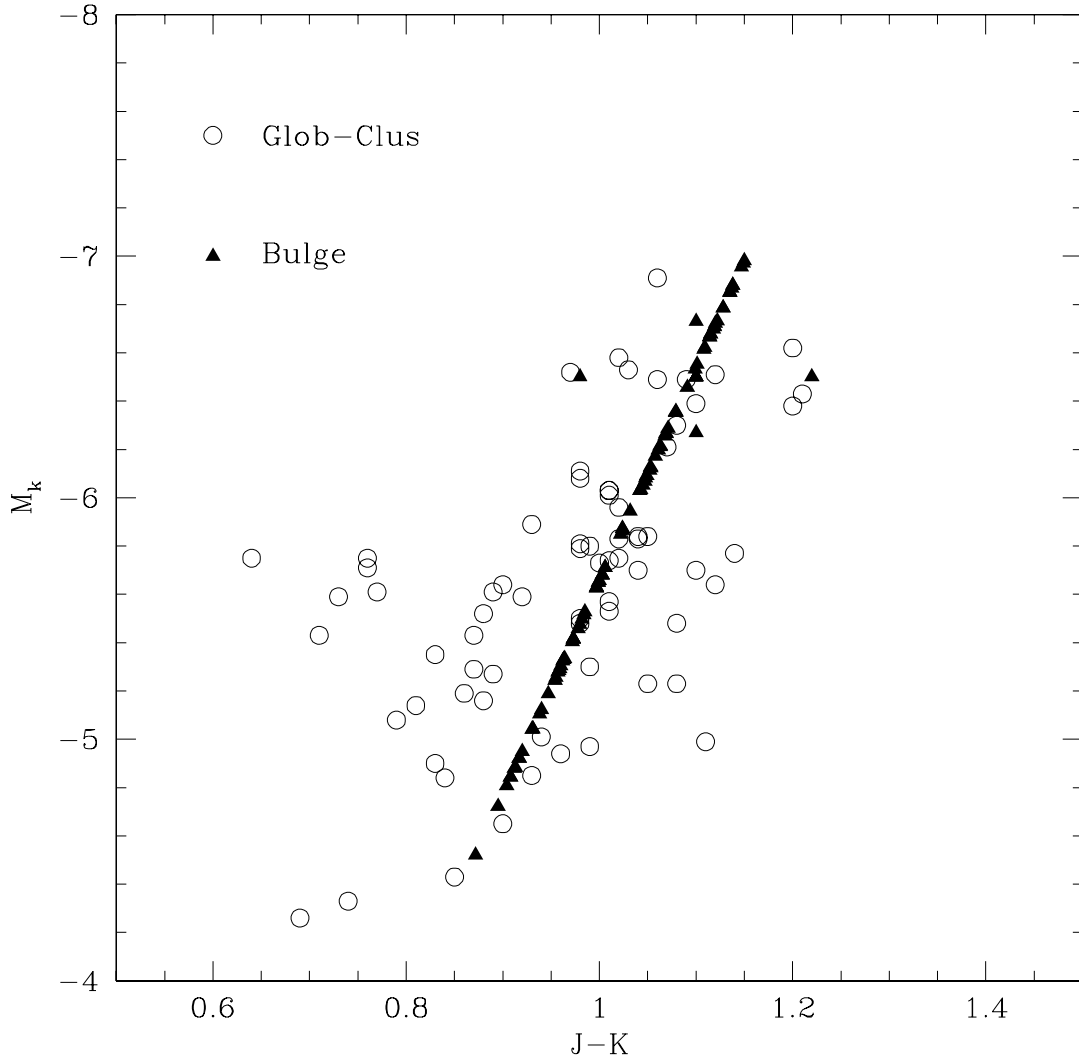


Fig. 3.— Color-Magnitude Diagram of bulge stars from this work (*filled-triangles*) and globular cluster stars from Stephens et al. (2000) (*open-circles*).

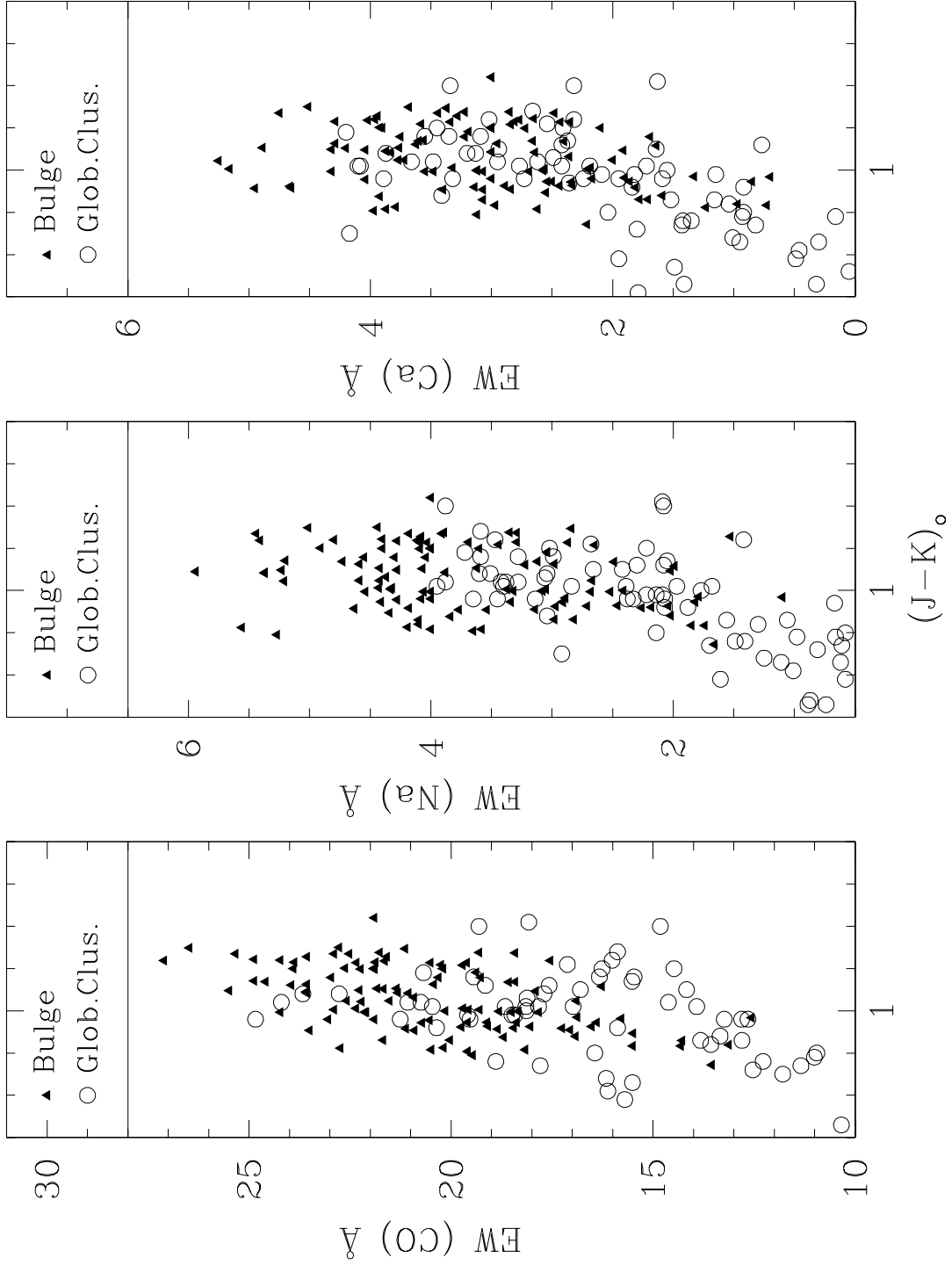


Fig. 4.— Equivalent widths of the spectral features Na, Ca, and CO plotted against color $(J-K)_0$. Bulge stars (*filled – triangles*) and globular cluster stars (*open – circles*) have similar spectral and photometric parameters.

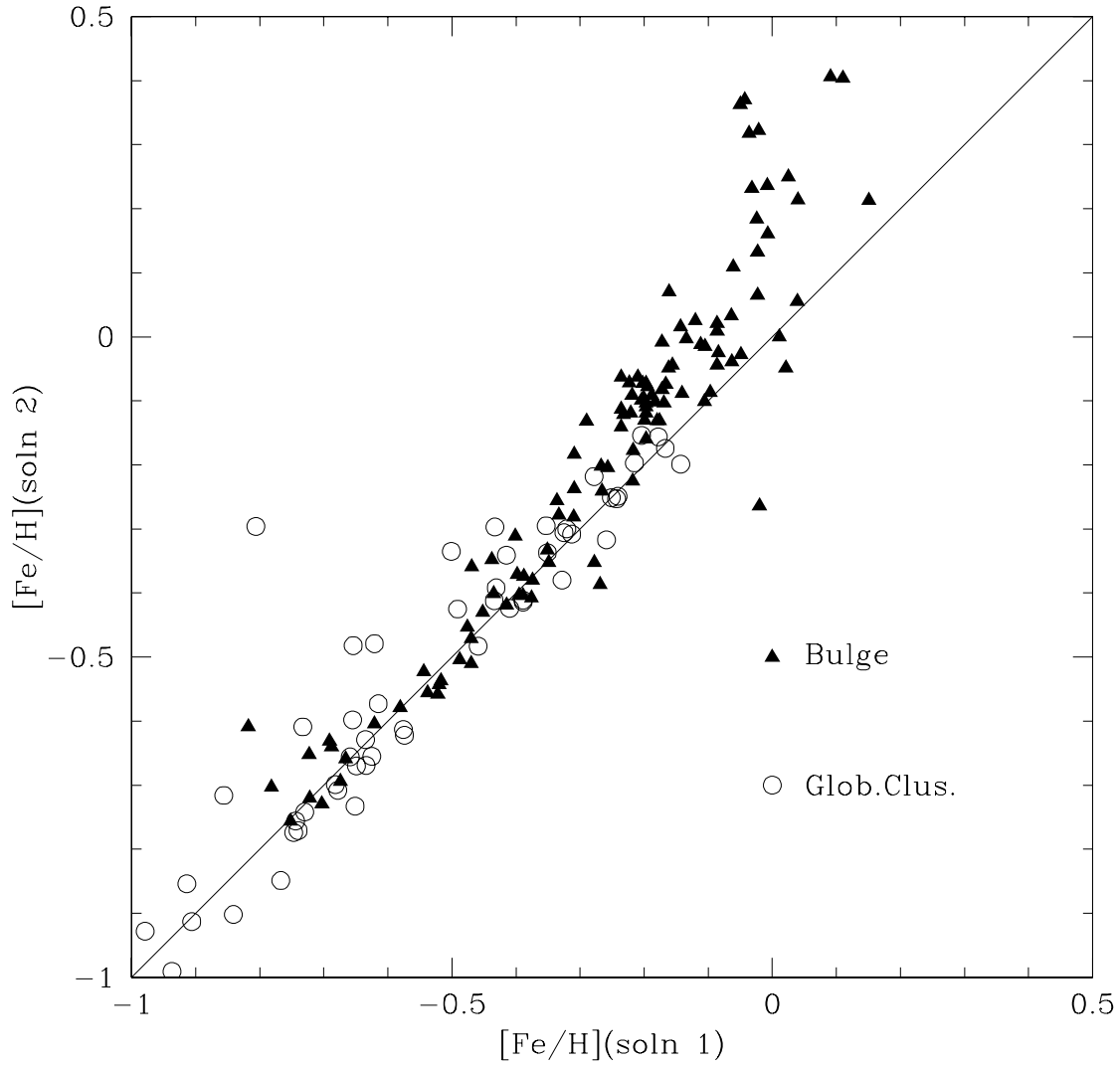


Fig. 5.— Metallicity from solution 1 and from solution 2 applied to bulge stars (*filled – triangles*) and globular cluster stars (*open – circles*).

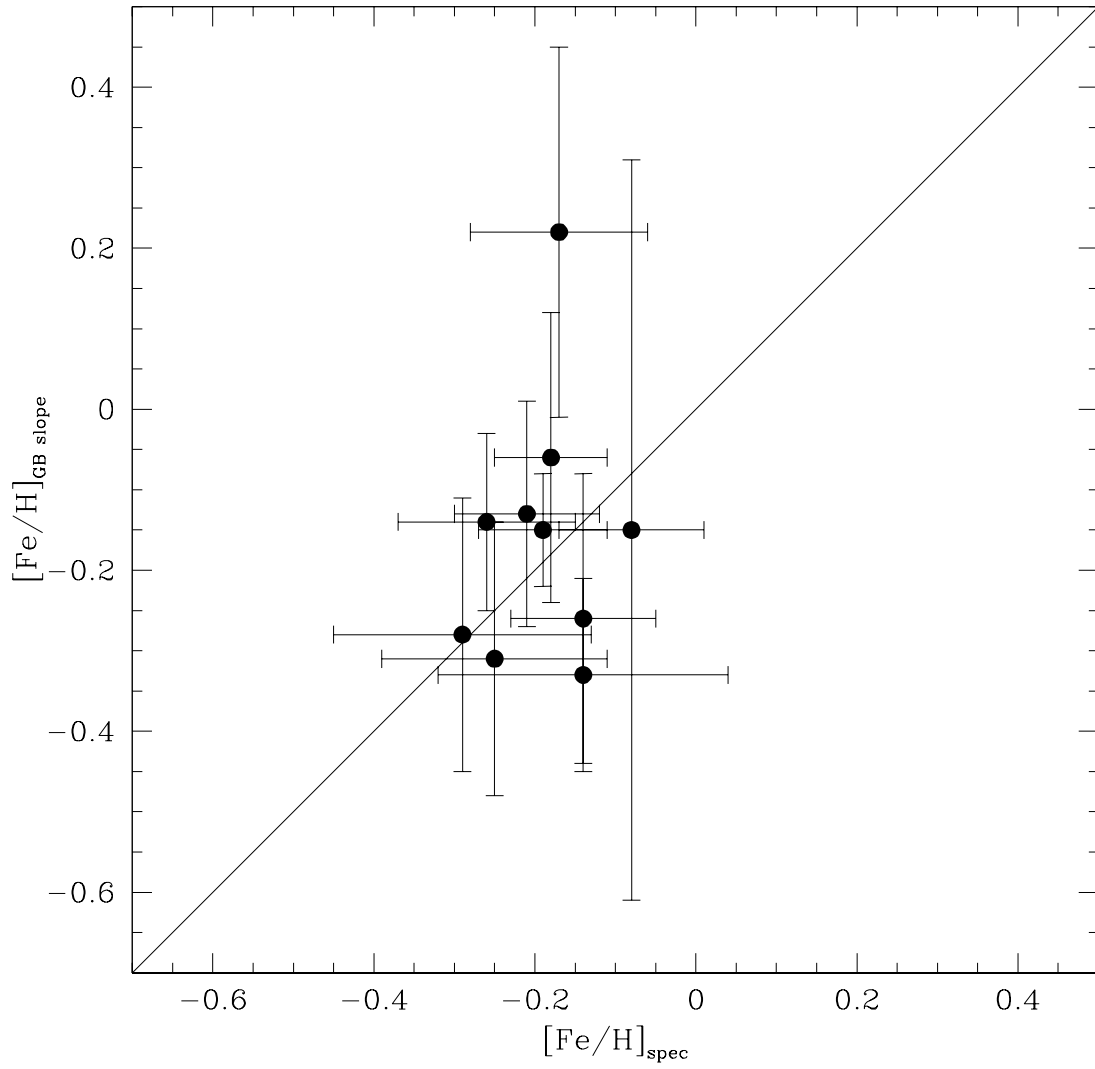


Fig. 6.— $[\text{Fe}/\text{H}]$ from our spectroscopic calibration plotted against $[\text{Fe}/\text{H}]$ from the slope of the giant branch (GB) from Frogel et al. (1999).

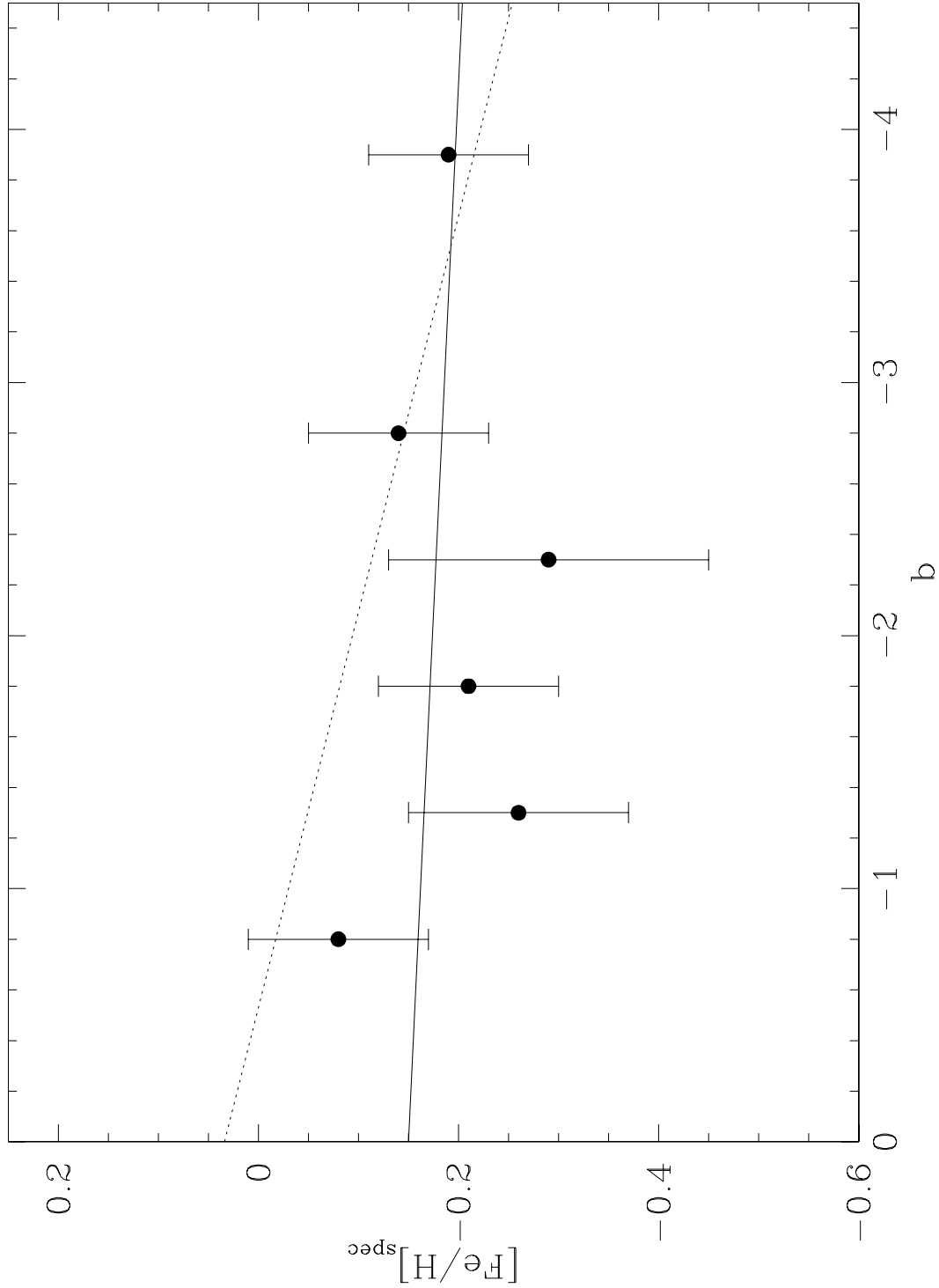


Fig. 7.— $[\text{Fe}/\text{H}]$ from our spectroscopic calibration plotted against galactic longitude, b for fields in the inner bulge with galactic latitude $b=1.3^\circ$. The line is an least-squares fit to the points. The slope of the line is 0.012 ± 0.018 dex/degree.

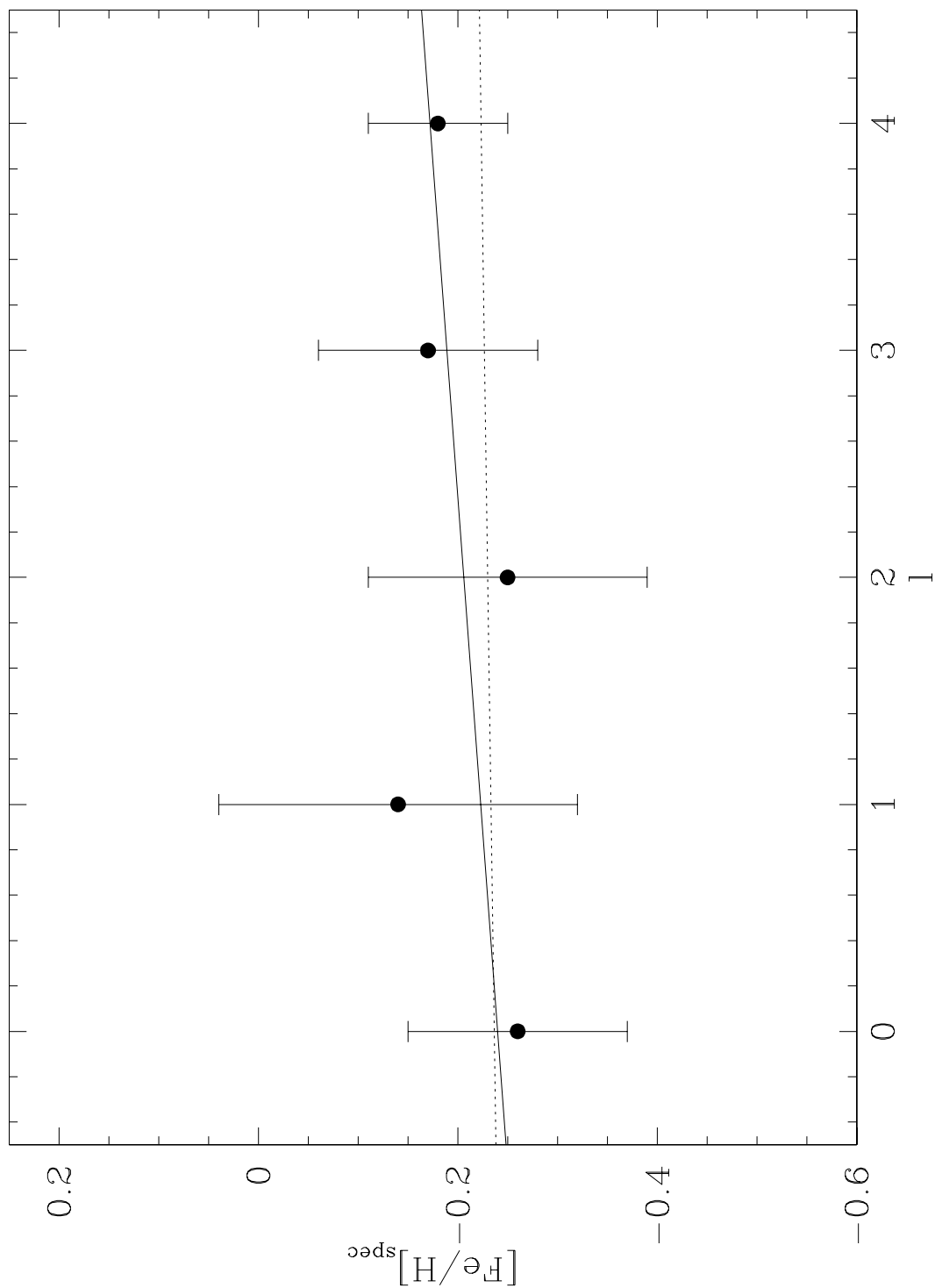


Fig. 8.— $[\text{Fe}/\text{H}]$ from our spectroscopic calibration plotted against galactic latitude, b for fields in the inner bulge with galactic longitude, $l \sim 0^\circ$. The line is an least-squares fit to the points. The slope of the line is -0.07 ± 0.05 dex/degree.

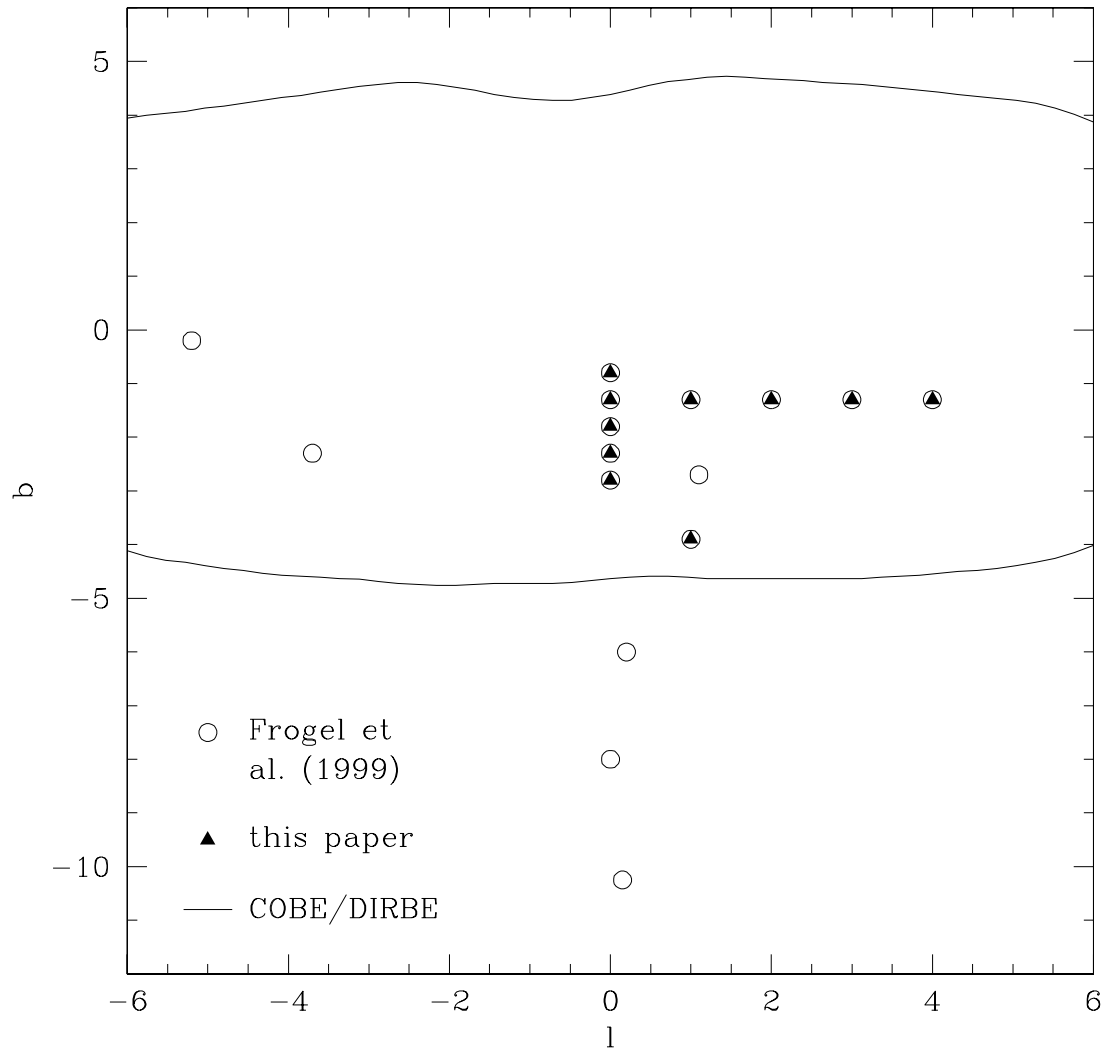


Fig. 9.— Location of observed fields with respect to the COBE/DIRBE $3.5 \mu\text{m}$ outline (*solid line*, Weiland et al. 1994) at 5 MJy sr^{-1} . The observed fields are from Frogel et al. (1999, *open - circles*) and this work (*filled - triangles*).

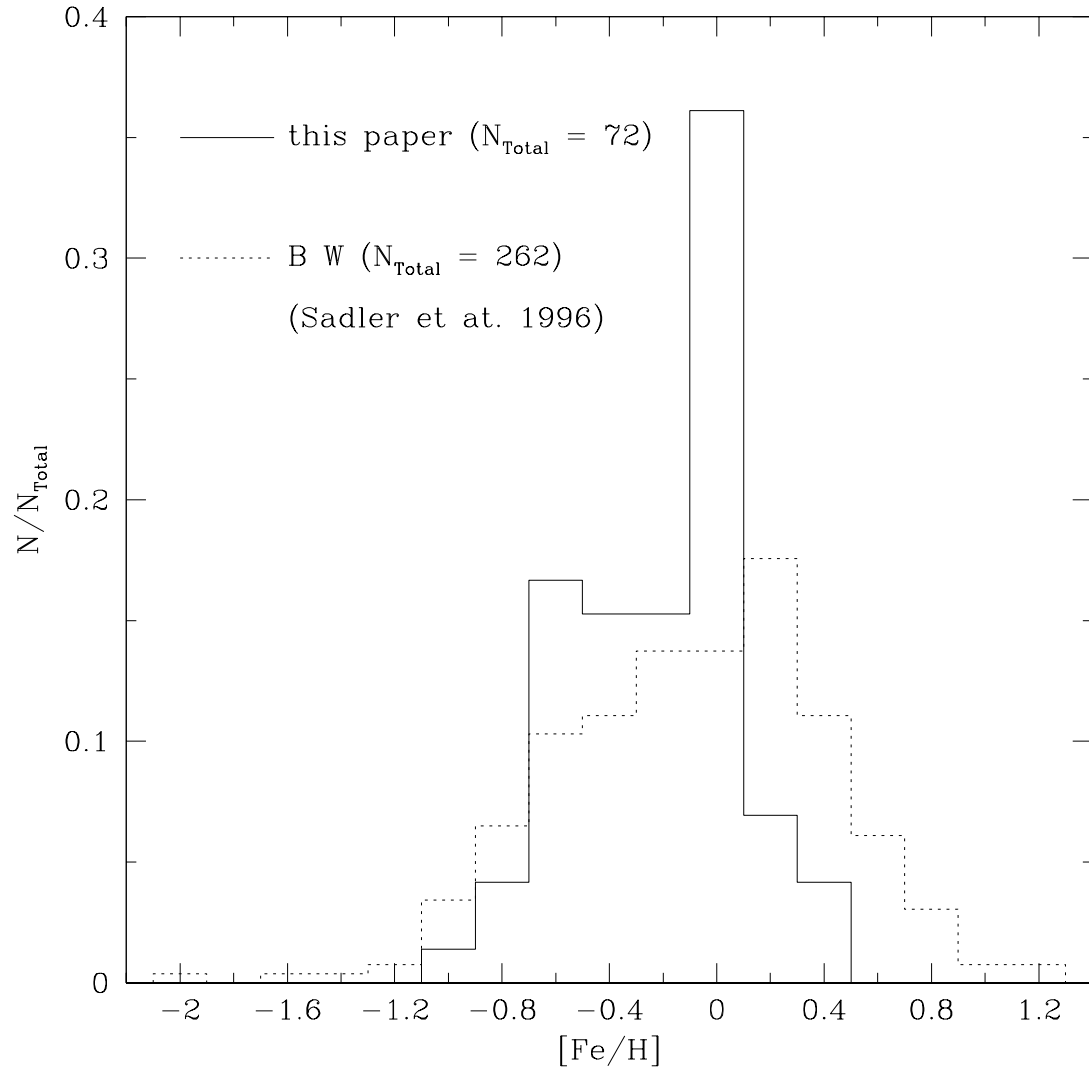


Fig. 10.— Fractional distribution of [Fe/H] for 86 inner bulge stars (*solid line*) compared to [Fe/H] fractional distribution for 262 Baade’s window stars (*dashed line*) from Sadler et al. (1996).

Table 1. Observations.

Date	Instrument	$\lambda/\Delta\lambda$
1993 August 26,27,28	OSIRIS	1380
1994 July 23,24,25,27,28	OSIRIS	1380
1995 July 19,20,21,22	IRS	1650 & 4830

Table 2: Observed Giant Stars.

Star	Date	$\lambda/\Delta\lambda$	S/N	K	J-K	M_{K_0}	(J-K) ₀	Na I (Å)	Ca I (Å)	¹² CO(2,0) (Å)
(1)	(2)	(3)	(4)	(5)	(6)	(7)	(8)	(9)	(10)	(11)
c1a3-03	940724	1380	91	9.63	2.61	-5.87	1.02	2.67 ± 0.19	2.00 ± 0.58	16.90 ± 0.50
c1a3-04	940724	1380	97	9.16	2.54	-6.27	1.07	3.12 ± 0.27	2.66 ± 0.47	18.41 ± 0.48
c1a3-06	940724	1380	78	8.91	2.93	-6.72	1.12	4.80 ± 0.32	3.96 ± 0.45	24.23 ± 0.70
c1a3-07	940724	1380	87	8.90	2.74	-6.62	1.11	3.44 ± 0.29	3.58 ± 0.40	20.25 ± 0.63
c1a3-08	940724	1380	57	9.65	2.96	-6.05	1.04	5.94 ± 0.54	3.87 ± 0.66	23.59 ± 0.83
c1a3-09	940724	1380	89	8.95	2.92	-6.68	1.12	3.69 ± 0.25	4.29 ± 0.34	23.88 ± 0.67
c1b1-01	940724	1380	133	8.69	2.39	-6.61	1.11	2.65 ± 0.17	2.84 ± 0.20	19.71 ± 0.46
c1b1-02	940724	1380	79	8.52	3.49	-7.41	1.20	3.80 ± 0.22	1.85 ± 0.46	24.69 ± 0.75
c1b1-04	940724	1380	81	8.15	2.92	-7.43	1.20	3.29 ± 0.31	2.66 ± 0.41	23.43 ± 0.69
c1b1-05	940724	1380	68	8.62	2.89	-6.97	1.15	5.01 ± 0.21	3.68 ± 0.69	26.48 ± 0.77
c1b1-10	940724	1380	48	8.85	2.94	-6.79	1.13	4.08 ± 0.23	3.28 ± 0.35	23.57 ± 1.44
c1b1-10	930828	1380	61	8.85	2.94	-6.79	1.13	1.53 ± 0.50	3.94 ± 0.42	21.59 ± 0.91
c1b1-23	940724	1380	68	9.51	2.78	-6.08	1.05	5.23 ± 0.46	4.04 ± 0.40	25.49 ± 0.80
c2b-09	950620	1650	83	8.65	4.85	-8.07	1.27	2.03 ± 0.22	1.34 ± 0.36	16.82 ± 0.68
c2b-10	950620	1650	47	8.90	4.91	-7.88	1.25	5.68 ± 0.50	1.30 ± 0.84	24.06 ± 0.99
c2b-43	950620	1650	25	10.02	4.97	-6.87	1.14	3.29 ± 0.91	-2.00 ± 1.87	18.42 ± 1.48
c2b-44	950620	1650	28	9.63	5.08	-7.30	1.18	5.59 ± 0.60	1.64 ± 1.70	20.97 ± 1.58
c2b-45	950620	1650	21	10.03	4.71	-6.71	1.12	4.11 ± 0.79	-3.16 ± 2.26	17.55 ± 1.96
c3a-05	930828	1380	50	9.67	3.37	-6.27	1.07	4.73 ± 0.42	3.60 ± 0.51	24.59 ± 1.22
c3a-12	930827	1380	53	9.22	4.43	-7.30	1.18	4.71 ± 0.30	3.20 ± 0.58	25.16 ± 1.18
c3a-15	930827	1380	47	9.65	4.34	-6.85	1.13	5.44 ± 0.40	4.75 ± 0.65	25.34 ± 1.29
c3a-17	930828	1380	49	9.33	4.26	-7.10	1.16	5.04 ± 0.35	4.05 ± 0.57	24.95 ± 1.29
c3a-18	930828	1380	58	8.78	4.01	-7.47	1.20	3.81 ± 0.24	2.58 ± 0.28	19.89 ± 1.18
c3a-20	930828	1380	31	9.57	4.72	-7.13	1.17	1.93 ± 0.78	-0.92 ± 1.16	27.27 ± 1.73
c3a-22	930828	1380	49	8.99	4.02	-7.28	1.18	2.25 ± 0.24	0.64 ± 0.47	15.09 ± 1.36
c3a-23	930828	1380	53	9.34	4.18	-7.05	1.16	4.71 ± 0.25	3.41 ± 0.44	24.89 ± 1.26
c3a-33	930827	1380	49	9.81	5.23	-7.21	1.17	3.79 ± 0.29	3.87 ± 0.72	20.67 ± 1.24
g0-1.3a-01	930826	1380	38	8.31	1.89	-6.68	1.12	3.29 ± 0.23	2.81 ± 0.33	21.87 ± 1.84
g0-1.3a-02	930826	1380	33	8.51	1.96	-6.53	1.10	4.09 ± 0.44	2.72 ± 0.65	22.24 ± 1.97
g0-1.3a-03	930826	1380	35	7.86	1.50	-6.88	1.14	3.35 ± 0.32	3.22 ± 0.25	19.31 ± 1.99
g0-1.3a-04	930826	1380	32	8.95	1.93	-6.11	1.05	4.07 ± 0.32	4.20 ± 0.63	21.67 ± 2.09
g0-1.3a-06	930826	1380	32	9.17	1.84	-5.85	1.02	5.21 ± 0.43	5.25 ± 0.51	22.22 ± 2.08

Star	Date	$\lambda/\Delta\lambda$	S/N	K	J-K	M_{K_0}	(J-K) ₀	Na I (Å)	Ca I (Å)	¹² CO(2,0) (Å)
(1)	(2)	(3)	(4)	(5)	(6)	(7)	(8)	(9)	(10)	(11)
g0-1.3a-14	930826	1380	36	9.67	1.71	-5.31	0.96	2.18 ± 0.28	3.14 ± 0.55	18.45 ± 1.91
g0-1.3a-15	930826	1380	32	9.65	1.71	-5.32	0.96	2.97 ± 0.39	4.66 ± 0.51	19.75 ± 2.13
g0-1.3a-16	930826	1380	38	9.62	1.81	-5.41	0.97	1.82 ± 0.25	2.54 ± 0.35	16.39 ± 1.84
g0-1.8a-01	950622	4830	52	9.11	1.46	-5.68	1.00	3.37 ± 0.24	2.56 ± 0.33	22.90 ± 0.52
g0-1.8a-01	950619	1650	83	9.11	1.46	-5.68	1.00	3.05 ± 0.21	2.20 ± 0.51	19.29 ± 0.59
g0-1.8a-03	950621	4830	53	7.67	1.58	-7.11	1.16	3.51 ± 0.30	2.69 ± 0.37	18.81 ± 0.42
g0-1.8a-03	950619	1650	64	7.67	1.58	-7.11	1.16	4.11 ± 0.34	4.07 ± 0.58	22.83 ± 0.77
g0-1.8a-04	950622	4830	43	9.56	1.42	-5.25	0.95	3.77 ± 0.34	3.07 ± 0.35	23.50 ± 0.61
g0-1.8a-04	950619	1650	71	9.56	1.42	-5.25	0.95	3.54 ± 0.28	3.40 ± 0.54	20.91 ± 0.70
g0-1.8a-05	950621	4830	32	9.24	1.58	-5.63	1.00	4.00 ± 0.45	3.55 ± 0.61	24.23 ± 0.73
g0-1.8a-05	950619	1650	76	9.24	1.58	-5.63	1.00	4.54 ± 0.26	3.48 ± 0.44	22.13 ± 0.70
g0-1.8a-10	950621	4830	30	9.86	1.56	-5.04	0.93	2.82 ± 0.41	1.78 ± 0.78	21.68 ± 0.74
g0-1.8a-10	950619	1650	74	9.86	1.56	-5.04	0.93	2.98 ± 0.34	1.71 ± 0.50	20.03 ± 0.64
g0-1.8a-13	950621	4830	22	9.97	1.53	-4.92	0.92	1.85 ± 0.66	2.97 ± 1.02	14.31 ± 0.97
g0-1.8a-13	950619	1650	74	9.97	1.53	-4.92	0.92	1.74 ± 0.41	0.73 ± 0.43	15.50 ± 0.61
g0-1.8b-01	950622	4830	42	7.76	1.57	-7.01	1.15	3.04 ± 0.38	0.72 ± 0.48	11.95 ± 0.52
g0-1.8b-01	950619	1650	63	7.76	1.57	-7.01	1.15	2.81 ± 0.46	1.25 ± 0.55	10.70 ± 0.70
g0-1.8b-02	950622	4830	36	8.86	1.65	-6.03	1.04	5.37 ± 0.37	2.64 ± 0.57	23.57 ± 0.68
g0-1.8b-02	950619	1650	50	8.86	1.65	-6.03	1.04	5.37 ± 0.37	3.83 ± 0.83	21.05 ± 0.95
g0-1.8b-03	950619	1650	60	7.82	1.45	-6.88	1.14	3.89 ± 0.48	2.85 ± 0.41	21.77 ± 0.86
g0-1.8b-07	950622	4830	60	9.39	1.44	-5.42	0.97	2.91 ± 0.19	1.86 ± 0.35	19.59 ± 0.43
g0-1.8b-07	950619	1650	75	9.39	1.44	-5.42	0.97	3.34 ± 0.32	2.50 ± 0.49	18.37 ± 0.65
g0-1.8b-10	950622	4830	40	9.92	1.32	-4.84	0.91	3.58 ± 0.35	2.62 ± 0.56	20.49 ± 0.56
g0-1.8b-10	950619	1650	64	9.92	1.32	-4.84	0.91	4.00 ± 0.41	3.87 ± 0.41	18.16 ± 0.83
g0-2.3a-01	950619	1650	49	9.17	1.26	-5.52	0.98	1.10 ± 0.31	0.70 ± 1.05	12.56 ± 0.80
g0-2.3a-02	950619	1650	57	9.37	1.51	-5.48	0.98	4.08 ± 0.36	2.17 ± 0.71	23.04 ± 0.84
g0-2.3a-03	950619	1650	81	9.07	1.07	-5.50	0.98	2.89 ± 0.23	1.90 ± 0.54	15.79 ± 0.58
g0-2.3a-04	950619	1650	67	10.10	1.39	-4.72	0.89	5.27 ± 0.42	3.12 ± 0.48	19.46 ± 0.72
g0-2.3b-01	950619	1650	61	7.49	1.73	-7.36	1.19	5.26 ± 0.29	4.24 ± 0.55	26.87 ± 0.90
g0-2.3b-02	950619	1650	68	8.15	1.66	-6.70	1.12	4.28 ± 0.30	4.02 ± 0.45	21.64 ± 0.81
g0-2.3b-03	950619	1650	55	7.84	1.64	-6.98	1.15	4.44 ± 0.29	4.51 ± 0.71	22.77 ± 0.92
g0-2.3b-05	950619	1650	96	9.43	1.30	-5.29	0.96	2.26 ± 0.24	1.81 ± 0.32	17.25 ± 0.55

Star	Date	$\lambda/\Delta\lambda$	S/N	K	J-K	M_{K_0}	(J-K) ₀	Na I (Å)	Ca I (Å)	¹² CO(2,0) (Å)
(1)	(2)	(3)	(4)	(5)	(6)	(7)	(8)	(9)	(10)	(11)
g0-2.3b-06	950619	1650	66	10.17	1.16	-4.52	0.87	1.66 ± 0.48	2.21 ± 0.49	13.55 ± 0.65
g0-2.8a-01	930826	1380	32	8.17	1.71	-6.71	1.12	5.41 ± 0.21	2.77 ± 0.52	27.11 ± 2.19
g0-2.8a-02	930826	1380	39	9.50	1.60	-5.41	0.97	2.91 ± 0.32	2.34 ± 0.31	20.72 ± 1.78
g0-2.8a-03	930826	1380	33	9.51	1.49	-5.34	0.96	2.46 ± 0.33	2.33 ± 0.42	19.09 ± 2.06
g0-2.8a-04	930827	1380	33	10.03	1.43	-4.81	0.90	3.65 ± 0.24	3.97 ± 0.53	19.59 ± 2.07
g0-2.8a-05	930826	1380	38	9.79	1.58	-5.12	0.94	2.02 ± 0.30	1.59 ± 0.26	16.92 ± 1.83
g0-2.8a-07	930827	1380	31	10.10	1.67	-4.88	0.91	4.19 ± 0.45	3.79 ± 0.49	20.18 ± 2.15
g0-2.8b-04	930827	1380	34	9.27	1.62	-5.63	1.00	4.06 ± 0.41	4.32 ± 0.41	22.10 ± 2.00
g0-2.8b-05	930827	1380	27	9.33	1.75	-5.65	1.00	3.32 ± 0.25	2.57 ± 0.69	18.81 ± 2.57
g0-2.8b-06	930827	1380	32	8.74	1.62	-6.13	1.05	3.62 ± 0.45	3.76 ± 0.65	21.35 ± 2.08
g1-1.3a-04	950622	4830	52	8.75	1.71	-6.17	1.06	1.99 ± 0.26	1.64 ± 0.44	16.27 ± 0.42
g1-1.3a-06	950620	1650	62	8.93	1.77	-6.04	1.04	3.88 ± 0.45	3.00 ± 0.59	21.32 ± 0.71
g1-1.3a-09	950620	1650	35	9.51	1.64	-5.42	0.97	4.41 ± 0.98	0.85 ± 0.90	19.11 ± 1.16
g1-1.3a-10	950620	1650	34	8.99	1.71	-5.94	1.03	4.37 ± 0.91	2.36 ± 1.08	20.92 ± 1.22
g1-1.3a-11	950620	1650	20	10.17	1.77	-4.88	0.91	5.56 ± 1.36	1.23 ± 1.90	22.74 ± 2.09
g2-1.3b-02	940727	1380	111	8.82	1.90	-6.21	1.06	2.98 ± 0.23	2.95 ± 0.35	20.43 ± 0.47
g2-1.3b-03	940727	1380	92	8.51	1.99	-6.55	1.10	4.91 ± 0.22	3.92 ± 0.32	22.62 ± 0.66
g2-1.3b-05	940727	1380	124	8.77	1.89	-6.26	1.07	2.49 ± 0.18	2.40 ± 0.40	18.57 ± 0.37
g2-1.3b-08	940727	1380	143	8.85	1.69	-6.07	1.05	2.02 ± 0.13	1.91 ± 0.34	17.90 ± 0.34
g2-1.3b-09	940727	1380	91	8.89	1.81	-6.09	1.05	4.28 ± 0.19	4.32 ± 0.38	22.27 ± 0.66
g2-1.3b-10	940727	1380	99	8.14	1.90	-6.85	1.13	4.18 ± 0.16	3.44 ± 0.36	22.52 ± 0.61
g3-1.3a-01	950620	1650	68	8.85	2.08	-6.29	1.07	5.20 ± 0.35	3.56 ± 0.47	24.88 ± 0.76
g3-1.3a-04	950620	1650	80	9.86	1.97	-5.28	0.96	4.63 ± 0.34	4.95 ± 0.25	18.84 ± 0.67
g3-1.3a-05	950620	1650	30	10.00	1.63	-4.95	0.92	4.10 ± 0.83	0.97 ± 1.44	13.13 ± 1.31
g3-1.3a-08	950620	1650	85	9.57	1.92	-5.53	0.99	1.79 ± 0.29	1.33 ± 0.55	16.88 ± 0.46
g3-1.3b-02	950620	1650	62	9.46	2.01	-5.68	1.00	4.33 ± 0.38	5.16 ± 0.62	19.57 ± 0.75
g3-1.3b-03	950620	1650	84	8.58	1.94	-6.46	1.09	3.04 ± 0.30	3.19 ± 0.45	19.38 ± 0.54
g3-1.3b-05	950620	1650	38	10.17	2.06	-5.04	0.93	4.10 ± 0.67	3.07 ± 1.10	14.28 ± 1.11
g3-1.3b-06	950620	1650	46	9.92	1.91	-5.19	0.95	4.34 ± 0.59	2.55 ± 0.89	15.49 ± 0.89
g4-1.3a-06	940723	1380	74	8.91	2.30	-6.36	1.08	4.30 ± 0.32	3.75 ± 0.53	22.97 ± 0.72
g4-1.3a-09	940723	1380	85	9.39	1.86	-5.66	1.00	2.41 ± 0.34	3.12 ± 0.49	20.14 ± 0.56
g4-1.3a-10	940723	1380	123	9.70	1.66	-5.26	0.95	3.14 ± 0.18	2.84 ± 0.20	17.05 ± 0.50

Star	Date	$\lambda/\Delta\lambda$	S/N	K	J-K	M_{K_0}	$(J-K)_0$	Na I (Å)	Ca I (Å)	$^{12}\text{CO}(2,0)$ (Å)
(1)	(2)	(3)	(4)	(5)	(6)	(7)	(8)	(9)	(10)	(11)
g4-1.3a-12	940723	1380	91	9.50	1.70	-5.46	0.98	4.28 ± 0.22	4.04 ± 0.39	20.53 ± 0.63
g4-1.3d-01	940724	1380	84	8.99	2.02	-6.13	1.05	4.42 ± 0.26	4.89 ± 0.46	21.83 ± 0.65
g4-1.3d-02	940724	1380	68	9.02	2.22	-6.22	1.06	4.59 ± 0.40	4.29 ± 0.49	23.57 ± 0.79
g4-1.3d-03	940724	1380	99	9.07	2.28	-6.20	1.06	3.22 ± 0.12	3.62 ± 0.40	23.95 ± 0.59
g4-1.3d-05	940724	1380	85	9.52	2.06	-5.65	1.00	3.08 ± 0.32	3.12 ± 0.50	18.33 ± 0.56
g4-1.3d-06	940724	1380	52	9.93	2.09	-5.28	0.96	4.18 ± 0.51	4.65 ± 0.81	21.12 ± 0.91
g4-1.3d-09	940724	1380	85	9.97	1.85	-5.11	0.94	3.84 ± 0.33	3.92 ± 0.34	18.70 ± 0.65
B-024	950621	4830	40	7.18	1.03	-7.24	1.18	4.18 ± 0.22	2.90 ± 0.58	24.25 ± 0.64
B-024	950619	1650	82	7.18	1.03	-7.24	1.18	3.96 ± 0.30	3.51 ± 0.33	20.81 ± 0.65
B-024	940724	1380	101	7.18	1.03	-7.24	1.18	3.71 ± 0.28	3.11 ± 0.31	23.67 ± 0.54
B-036	950620	1650	71	8.80	1.00	-5.71	1.01	4.32 ± 0.41	2.18 ± 0.44	19.70 ± 0.66
B-036	940724	1380	82	8.80	1.00	-5.71	1.01	4.43 ± 0.28	3.32 ± 0.33	22.35 ± 0.74
B-064	950620	1650	91	9.17	0.94	-5.33	0.96	2.71 ± 0.33	2.89 ± 0.36	18.04 ± 0.49
B-064	940726	1380	97	9.17	0.94	-5.33	0.96	2.04 ± 0.33	2.44 ± 0.44	16.52 ± 0.43
B-066	950620	1650	87	8.79	0.84	-5.63	1.00	2.68 ± 0.26	3.07 ± 0.51	17.83 ± 0.49
B-066	940726	1380	107	8.79	0.84	-5.63	1.00	2.52 ± 0.37	2.69 ± 0.16	18.50 ± 0.45
B-069	950621	4830	48	7.79	1.02	-6.67	1.11	4.09 ± 0.20	2.35 ± 0.42	22.34 ± 0.57
B-069	950619	1650	79	7.79	1.02	-6.67	1.11	4.03 ± 0.24	2.43 ± 0.46	19.61 ± 0.66
B-069	940726	1380	92	7.79	1.02	-6.67	1.11	2.87 ± 0.31	3.34 ± 0.45	20.51 ± 0.52
B-070	950619	1650	53	8.64	1.02	-5.87	1.02	4.42 ± 0.32	3.77 ± 0.77	21.52 ± 0.94
B-070	940725	1380	89	8.64	1.02	-5.87	1.02	4.59 ± 0.22	3.72 ± 0.42	22.58 ± 0.64
B-124	950619	1650	52	8.23	1.19	-6.35	1.08	4.55 ± 0.35	1.69 ± 0.74	19.26 ± 0.99
B-124	940726	1380	66	8.23	1.19	-6.35	1.08	4.04 ± 0.55	3.22 ± 0.37	20.31 ± 0.76
B-138	950621	4830	32	6.70	1.28	-7.84	1.25	5.31 ± 0.30	2.51 ± 0.75	24.89 ± 0.74
B-138	950619	1650	61	6.70	1.28	-7.84	1.25	5.19 ± 0.30	3.62 ± 0.65	24.06 ± 0.81
B-138	940724	1380	67	6.70	1.28	-7.84	1.25	4.77 ± 0.30	3.96 ± 0.41	25.19 ± 0.93
BMB-028	940725	1380	88	7.37	1.37	-7.26	1.18	3.94 ± 0.21	3.10 ± 0.30	22.93 ± 0.72
BMB-055	940726	1380	82	7.76	1.29	-6.85	1.13	3.91 ± 0.30	2.48 ± 0.43	22.90 ± 0.67
BMB-078	940725	1380	114	7.50	1.05	-6.96	1.15	2.84 ± 0.21	3.37 ± 0.34	21.14 ± 0.46
BMB-205	940726	1380	68	7.58	1.38	-7.07	1.16	4.89 ± 0.42	3.41 ± 0.54	26.49 ± 0.75
BMB-247	940726	1380	81	7.83	1.20	-6.73	1.12	4.40 ± 0.35	2.65 ± 0.40	24.87 ± 0.66
BMB-289	940726	1380	75	6.03	1.28	-8.46	1.32	4.36 ± 0.39	2.35 ± 0.49	23.96 ± 0.68

Table 3. Definitions of band edges for continuum and features.

Feature Name	band edges (μm)
Na continuum # 1	2.191 – 2.197
Na continuum # 2	2.213 – 2.217
Na I feature	2.204 – 2.211
Ca continuum # 1	2.245 – 2.256
Ca continuum # 2	2.270 – 2.272
Ca I feature	2.258 – 2.269
$^{12}\text{CO}(2,0)$ continuum #1	2.190 – 2.201
$^{12}\text{CO}(2,0)$ continuum #2	2.211 – 2.222
$^{12}\text{CO}(2,0)$ continuum #3	2.233 – 2.260
$^{12}\text{CO}(2,0)$ continuum #4	2.268 – 2.280
$^{12}\text{CO}(2,0)$ continuum #5	2.286 – 2.291
$^{12}\text{CO}(2,0)$ bandhead	2.292 – 2.303

Table 4. Average differences in EW.

	$\Delta(\text{IRS}_{4830} - \text{IRS}_{1650})$ N=13		$\Delta(\text{IRS}_{1650} - \text{OSIRIS}_{1380})$ N=8		N=150
	Mean Δ	Standard Deviation	Mean Δ	Standard Deviation	<Formal error>
EW(Na)	-0.06	0.32	-0.36	0.43	0.34
EW(Ca)	-0.33	0.96	0.33	0.78	0.54
EW(CO)	1.50	2.10	1.10	1.30	1.04

Table 5. Standard Deviations of Equivalent Widths in two ranges of M_{K_0}

	$-6 \leq M_{K_0} \leq -7$	$-5 \leq M_{K_0} \leq -6$	Total Uncertainties
EW	σ	σ	σ
Na	0.98	0.95	0.38
Ca	0.98	0.95	0.87
CO	2.40	2.52	1.70

Table 6. Metallicity.

Field	N	$\langle[\text{Fe}/\text{H}]\rangle$	σ	Error in Mean
c	14	-0.08	0.33	0.09
g0-1.3	8	-0.26	0.28	0.11
g0-1.8	9	-0.21	0.25	0.09
g0-2.3	8	-0.29	0.42	0.16
g0-2.8	9	-0.14	0.25	0.09
g1-1.3	5	-0.14	0.35	0.18
g2-1.3	6	-0.25	0.32	0.14
g3-1.3	8	-0.17	0.28	0.11
g4-1.3	10	-0.18	0.20	0.07
BW	9	-0.19	0.21	0.07